Signal epidetection in third-harmonic generation microscopy of turbid media

Delphine Débarre,[1,2] Nicolas Olivier,[1] and Emmanuel Beaurepaire[1]

[1]*Laboratoire d'optique et biosciences, Ecole Polytechnique, CNRS, F-91128 Palaiseau, France, and INSERM U696, Palaiseau, France*

[2]*Current address: department of engineering science, University of Oxford, UK*

delphine.debarre@polytechnique.edu, nicolas.olivier@polytechnique.edu, emmanuel.beaurepaire@polytechnique.edu

Abstract: Third-harmonic generation (THG) imaging of thick samples or large organisms requires TH light to be epicollected through the focusing objective. In this study we first estimate the amount of backward-to-forward TH radiation created by an isolated object as a function of size and spatial frequencies in the object. Theory and model experiments indicate that no significant signal can be epidetected from a (biological) dielectric structure embedded in a transparent medium. In contrast, backward emission is observed from metal nanoparticles where THG is partly a surface effect. We then address the case of an object embedded in a turbid medium. Experiments and Monte Carlo simulations show that epidetection is possible when the absorption mean free path of harmonic light in the medium exceeds its reduced scattering length, and that epicollection efficiency critically depends on the microscope field-of-view even at shallow depths, because backscattered light is essentially diffusive. These observations provide guidelines for optimizing epidetection in third-harmonic, second-harmonic, or CARS imaging of thick tissues.

OCIS codes: (170.3880) Medical and biomedical imaging; (190.4160) Multiharmonic generation; (180.6900) Three-dimensional microscopy; (290.7050) Turbid media.

References and links

1. W. R. Zipfel, R. M. Williams and W. W. Webb, "Nonlinear magic:multiphoton microscopy in the biosciences," Nat. Biotechnol. **21**, 1369-1377 (2003)
2. K. Svoboda, W. Denk, D. Kleinfeld and D. W. Tank, "In vivo dendritic calcium dynamics in neocortical pyramidal neurons," Nature **385**, 161-165 (1997)
3. F. Helmchen and W. Denk, "New developments in multiphoton microscopy", Curr. Opin. Neurobiol. **12**, 593-601 (2002)
4. S. Charpak, J. Mertz, E. Beaurepaire, L. Moreaux and K. Delaney, "Odor-evoked calcium signals in dendrites of rat mitral cells," Proc. Nat. Acad. Sci. USA **98**, 1230-1234 (2001)
5. M. D. Cahalan, I. Parker, S. H. Wei and M. J. Miller, "Real-time imaging of lymphocytes in vivo," Curr. Opin. Immunol. **15**, 372-377 (2003)
6. S. Hugues, L. Fetler, L. Bonifaz, J. Helft, F. Amblard and S. Amigorena, "Distinct T cell dynamics in lymph nodes during the induction of tolerance and immunity," Nat. Immunol. **5**, 1235-42 (2004)
7. W. Wang, J. B. Wyckoff, V. C. Frohlich, Y. Oleynikov, S. Huttelmaier, J. Zavadil, L. Cermak, E. P. Bottinger, R. H. Singer, J. G. White, J. E. Segall and J. S. Condeelis, "Single cell behavior in metastatic primary mammary tumors correlated with gene expression patterns revealed by molecular profiling," Cancer Res. **62**, 6278-88 (2002)
8. J. M. Squirrell, D. L. Wokosin, J. G. White and B. D. Bavister, "Long-term two photon fluorescence imaging of mammalian embryos without compromising viability," Nat. Biotechnol. **17**, 763-767 (1999)
9. W. Supatto, D. Débarre, B. Moulia, E. Brouzés, J.-L. Martin, E. Farge and E. Beaurepaire, "*In vivo* modulation of morphogenetic movements in *Drosophila* embryos with femtosecond laser pulses," Proc. Nat. Acad. Sci. USA **102**, 1047-1052 (2005)
10. E. Beaurepaire and J. Mertz, "Epifluorescence collection in two-photon microscopy," Appl. Opt. **41**, 5376-5382 (2002)
11. M. Oheim, E. Beaurepaire, E. Chaigneau, J. Mertz and S. Charpak, "Two-photon microscopy in brain tissue: parameters influencing the imaging depth," J. Neurosci. Methods **111**, 29-37 (2001)

#83793 - $15.00 USD Received 4 Jun 2007; revised 16 Jun 2007; accepted 22 Jun 2007; published 3 Jul 2007

12. D. Vučinić, T. M. Bartol Jr. and T. J. Sejnowski, "Hybrid reflecting objectives for functional multiphoton microscopy in turbid media," Opt. Lett. **31**, 2447-2449 (2006)
13. Y. Barad, H. Eisenberg, M. Horowitz and Y. Silberberg, "Nonlinear scanning laser microscopy by third harmonic generation," Appl. Phys. Lett. **70**, 922-924 (1997)
14. M. Müller, J. Squier, K. R. Wilson and G. J. Brakenhoff, "3D-microscopy of transparent objects using third-harmonic generation," J. Microsc. **191**, 266-274 (1998)
15. D. Yelin and Y. Silberberg, "Laser scanning third-harmonic generation microscopy in biology," Opt. Express **5** (1999)
16. D. Oron, D. Yelin, E. Tal, S. Raz, R. Fachima and Y. Silberberg, "Depth-resolved structural imaging by third-harmonic generation microscopy," J. Struct. Biol. **147**, 3-11 (2004)
17. D. Débarre, W. Supatto, E. Farge, B. Moulia, M.-C. Schanne-Klein and E. Beaurepaire, "Velocimetric third-harmonic generation microscopy: micrometer-scale quantification of morphogenetic movements in unstained embryos," Opt. Lett. **29**, 2881-2883 (2004)
18. D. Débarre, W. Supatto, A.-M. Pena, A. Fabre, T. Tordjmann, L. Combettes, M.-C. Schanne-Klein and E. Beaurepaire, "Imaging lipid bodies in cells and tissues using third-harmonic generation microscopy," Nat. Methods **3**, 47-53 (2006)
19. C.-K. Sun, C.-C. Chen, S.-W. Chu, T.-H. Tsai, Y.-C. Chen and B.-L. Lin, "Multiharmonic generation biopsy of skin," Opt. Lett. **28**, 2488-2490 (2003)
20. S.-P. Tai, W.-J. Lee, D.-B.Shieh, P.-C. Wu, H.-Y. Huang, C.-H. Yu and C.-K. Sun, "In vivo optical biopsy of hamster oral cavity with epi-third-harmonic generation microscopy," Opt. Express **14**, 6178-6187 (2006)
21. J.-X. Cheng and X. S. Xie, "Green's function formulation for third harmonic generation microscopy," J. Opt. Soc. Am. B **19**, 1604-1610 (2002)
22. L. Moreaux, O. Sandre and J. Mertz, "Membrane imaging by second-harmonic generation microscopy," J. Opt. Soc. Am. B **17**, 1685-1694 (2000)
23. J. Mertz and L. Moreaux, "Second-harmonic generation by focused excitation of inhomogeneously distributed scatterers," Opt. Commun. **196**, 325-330 (2001)
24. R. M. Williams, W. R. Zipfel and W. W. Webb, "Interpreting second-harmonic images of collagen I fibrils," Biophys. J. **88**, 1377-1386 (2005)
25. O. Nadiarnykh, R. Lacomb, P. J. Campagnola and W. A. Mohler, "Coherent and incoherent SHG in fibrillar cellulose matrices," Opt. Express **15**, 3348-3360 (2007)
26. J.-X. Cheng, A. Volkmer and X. S. Xie, "Theoretical and experimental characterization of coherent anti-Stokes Raman scattering microscopy," J. Opt. Soc. Am. B **19**, 1328-1347 (2002)
27. C. L. Evans, E. O. Potma, M. Puoris'haag, D. Côté, C. P. Lin and X. S. Xie, "Chemical imaging of tissue in vivo with video-rate coherent anti-STokes Raman scattering microscopy," Proc. Nat. Acad. Sci. USA **102**, 16807-12 (2005)
28. R. W. Boyd, *Nonlinear optics, 2nd edition*, (Academic Press, 2003)
29. S.-P. Tai, T.-H. Tsai, W.-J. Lee, D.-B. Shieh, Y.-H. Liao, H.-Y. Huang, K. Y. J. Zhang, H.-L. Liu and C.-K. Sun, "Optical biopsy of fixed human skin with backward-collected optical harmonics signals," Opt. Express **13**, 8231-8242 (2005)
30. D. Débarre, W. Supatto and E. Beaurepaire, "Structure sensitivity in third-harmonic generation microscopy", Opt. Lett. **30**, 2134-2136 (2005)
31. B. Richards and E. Wolf, "Electromagnetic diffraction in optical systems II. Structure of the image field in an aplanetic system," Proc. Royal Soc. A **253**, 358-379 (1959)
32. M. Lippitz M. A. van Dijk.and M. Orrit, "Third-harmonic generation from single gold nanoparticules," Nano Lett. **5**, 799-802 (2005)
33. S. V. Popruzhenko, D. F. Zaretsky and W. Becker, "Third-harmonic generation by small clusters in a dielectric medium," J. Phys. B: At. Mol. Opt. Phys. **39**, 4933-4943 (2006)
34. J. J. Mock, M. Barbic, D. R. Smith, D. A. Schultz and S. Schultz, "Shape effects in plasmon resonance of individual silver nanoparticles," J. Chem. Phys. **116**, 6755-6759 (2002)
35. M. H. Niemz, *Laser-tissue interactions - Fundamentals and applications - Third Edition*, (Springer, 2004)
36. S. A. Prahl, M. Keijzer, S. L. Jacques and A. J. Welch, "A Monte Carlo model of light propagation in tissue," SPIE Institute Series **5**, 102-111 (1989)
37. C. G. Bohren and D. R. Huffman, *Absorption and scattering of light by small particles*, (Wiley, New York, 1983)
38. V. Barzda, C. Greenhalgh, J. Aus-der-Au and S. Elmore, "Visualization of mitochondria in cardiomyocytes by simultaneous harmonic generation and fluorescence microscopy," Opt. Express **13**, 8263-8276 (2006)
39. O. G. Clay, A. C. Millard, C. B. Schaffer, J. Aus-Der-Au, P. S. Tsai, J. A. Squier and D. Kleinfeld, "Spectroscopy of third harmonic generation: evidence for resonances in model compounds and ligated hemoglobin," J. Opt. Soc. Am. B **23**, 932-950 (2006)
40. N. Djaker, D. Gachet, N. Sandeau, P.-F. Lenne and H. Rigneault, "Refractive effects in coherent anti-Stokes Raman scattering microscopy," Appl. Opt. **45**, 7005-7011 (2006)

#83793 - $15.00 USD Received 4 Jun 2007; revised 16 Jun 2007; accepted 22 Jun 2007; published 3 Jul 2007

1. Introduction

One principal application of nonlinear microscopy in the life sciences is its use as a minimally invasive tool to study thick samples such as intact organs or small organisms at the micrometer scale [1]. Examples include in situ imaging of neuronal and vascular activity in intact brain [2-4], physiological studies in immunology [5, 6] and cancer [7], or long-term imaging of developing embryos [8, 9]. For many of these applications, epicollection of the signal through the focusing objective is required due to sample thickness. A handful of studies addressed the issue of optimizing the collection of multiphoton-excited fluorescence generated inside a scattering sample such as a biological tissue [10-12]. However the situation is different in the case of coherent nonlinear imaging (i.e. based on contrast mechanisms such as coherent anti-Stokes Raman scattering (CARS), second-, or third-harmonic generation (SHG, THG)). Unlike fluorescence, coherent nonlinear emission patterns are prescribed by the geometries of the sample and of the excitation beam. Emission is directional and often copropagating with the excitation beam, but may subsequently be affected by incoherent scattering. The description of coherent nonlinear imaging in a turbid medium therefore deserves a specific treatment.

In this study, we focus on THG microscopy [13], a technique recently demonstrated for imaging biological samples with three-dimensional resolution [9, 14-20] and providing information complementary to two-photon excited fluorescence (2PEF) and SHG microscopies. The forward/backward emission patterns in THG microscopy of complex media have received relatively little attention [21], compared to SHG [22-25] and CARS [26, 27] microscopy. Although theoretical considerations predict a negligible fraction of backward-emitted TH light in model situations [21, 28], a few studies reported the experimental observation of significant epidetected THG from samples such as skin biopsy [19, 29], oral mucosa [20] or lung tissue [18].

Here, we address the origin of this epidetected signal and discuss the conditions in which it can be efficiently detected. First, we numerically investigate the backward-to-forward third-harmonic emission ratio for model sample geometries, following the framework proposed by Cheng & Xie [21]. In particular, we discuss the incidence of axial spatial frequencies in the object [23] on coherent backward TH emission. These calculations and corresponding experiments in model samples indicate that THG from detectable heterogeneities is largely forward-directed, except in the case of surface-enhanced emission and in some periodic structures. We then analyze the influence of incoherent scattering and absorption of this TH emission by a surrounding turbid medium using Monte-Carlo simulations, and show that for a sample with limited absorption at the harmonic frequency, a significant fraction of backscattered forward-emitted light can be epicollected through the focusing objective. We investigate the impact of experimental parameters such as objective field-of-view and numerical aperture on TH epicollection efficiency, which turns out to differ from fluorescence epidetection. Finally, we corroborate this analysis by experiments on model and biological samples.

2. Coherent signal buildup in THG microscopy

Let us first summarize contrast generation in THG microscopy [13, 21, 28, 30], before addressing backward emission issues. Due to their coherence, harmonic waves created at different locations within the focal volume interfere to create the far-field detected signal. TH emission therefore depends on the geometries of the sample and of the excitation field. TH emission efficiency in a given direction (Θ,Φ) with respect to the optical axis (see Fig. 1) is governed by the wave vector mismatch $\Delta\mathbf{k}(\Theta,\Phi) = 3(\mathbf{k}_\omega+\mathbf{k}_g)-\mathbf{k}_{3\omega}$ [21] between the fundamental and harmonic waves inside the sample, arising from the Gouy phase shift experienced by the fundamental wave around the focal point (described by the wavevector $\mathbf{k}_g$) and from the medium dispersion between the harmonic and fundamental frequencies. Here $\mathbf{k}_\omega$ (resp. $\mathbf{k}_{3\omega}$) describes the wave vector of the fundamental (resp. harmonic) wave. In the following we restrict ourselves to dielectric, non birefringent, normally dispersive media

#83793 - $15.00 USD Received 4 Jun 2007; revised 16 Jun 2007; accepted 22 Jun 2007; published 3 Jul 2007

($3\|\mathbf{k}_\omega\| - \|\mathbf{k}_{3\omega}\| \leq 0$), which is relevant to most biological samples. Since the projection of $\mathbf{k}_g$ on the optical axis is negative, phase matching cannot be obtained in a homogeneous medium, and far-field emission is observable only if spatial frequencies are present in the sample that can compensate for $\Delta\mathbf{k}(\Theta,\Phi)$.

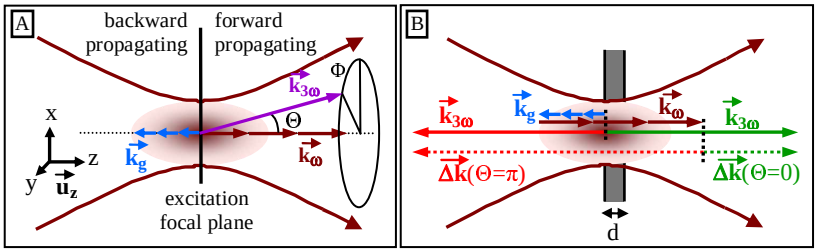

Fig. 1. (A) Geometry and notations (see text). (B) Wave vector mismatch in the forward and backward direction. A slab-like sample is shown for illustrative purpose (see discussion).

We estimated the forward/backward emission patterns for simple isolated objects using a Green's function formulation as proposed by Cheng & Xie [21], extended to take into account refractive index dispersion. The signal field produced at a position **R** in the collection optics aperture can be expressed as:

$$\mathbf{E}^{(\mathrm{THG})}(\mathbf{R}) \propto \iiint_V dV \left(\hat{\mathbf{I}} + \frac{\nabla\nabla}{k_3^{\,2}}\right) \frac{\exp\left(ik_3|\mathbf{R}-\mathbf{r}|\right)}{4\pi|\mathbf{R}-\mathbf{r}|} \cdot \mathbf{P}^{(3\omega)}(\mathbf{r}) \qquad (1)$$

where V is the sample volume, $\hat{\mathbf{I}}$ is a 3×3 unit matrix, k_3 is the third-harmonic wave vector amplitude and $\mathbf{P}^{(3\omega)}(\mathbf{r})$ is the third-order polarization at position **r**. For simplicity we further assumed a focused Gaussian beam shape with linear polarization for the excitation [28], although this approximation is not fully justified for high numerical apertures (NA=1.4). We verified the validity of that hypothesis by comparing the results obtained for the size-dependent forward emission of a sphere centered on the beam focus with estimates [21] based on the angular spectrum representation [31]. We find that the focused Gaussian beam approximation provides qualitatively similar results with only slight differences in the shape of the curve obtained; in particular, the sphere size that produces maximum THG is correctly predicted [30]. We then used this model to calculate the angular emission patterns from various sample geometries and the ratio of forward- to backward- TH radiation, defined by the integration of the TH emission over two half-spheres corresponding to $0 \leq \Theta \leq \pi/2$ and $\pi/2 \leq \Theta \leq \pi$ (Fig. 1A). Unless otherwise stated, all calculations assume an excitation wavelength of 1180 nm and linear indexes equal to those of water (1.325 at 1180 nm and 1.345 at 393 nm)

3. Emission patterns of isolated objects

3.1 THG from an interface

Table 1 summarizes the forward/backward ratios for an interface separating two homogenous, isotropic and semi-infinite media, excited under various focusing conditions. In all cases, the backward-propagating TH signal is much weaker than its forward counterpart.

We introduce a simple interpretation of this phenomenon in terms of the wave vector mismatch between the fundamental and harmonic waves and its compensation by the axial frequency spectrum of the object [23]: figure 2 illustrates the spatial frequencies present in the sample, schematized as a Heaviside function. In the case of an interface perpendicular to the optical axis z, the Fourier spectrum of the sample along the z direction contains all spatial frequencies with amplitude inversely proportional to the frequency. Therefore wave vector mismatch can be compensated both in the forward and the backward directions, albeit with efficiency depending on the amplitude of the corresponding spatial frequency component. Emission is thus orders of magnitude higher in the forward than in the backward direction

#83793 - $15.00 USD Received 4 Jun 2007; revised 16 Jun 2007; accepted 22 Jun 2007; published 3 Jul 2007

because $\Delta\mathbf{k}(\Theta=\pi)$ is much greater than $\Delta\mathbf{k}(\Theta=0)$. We note that the forward-to-backward emission ratio decreases for higher NAs (Table 1). This is interpreted simply by noting that $\|\mathbf{k}_g\|$ roughly scales as NA^2; when $\|\mathbf{k}_g\|$ is increased as a consequence of tighter focusing, the resulting wave-vector mismatch is increased in the forward direction and decreased in the backward direction (see fig 1B).In the case of an interface parallel to the optical axis z, only the null spatial frequency is present in the z direction, and no TH emission is obtained unless $\Delta\mathbf{k}(\Theta,\Phi).\mathbf{u}_z=0$, where $\mathbf{u}_z$ is the unit vector along axis z (fig. 1A). As noted previously, forward emission is deflected from the optical axis as a consequence of $\mathbf{k}_g$ [21], as for membrane SHG imaging [22]. In contrast, no TH light is radiated in the backward direction (Table 1).

Table 1. Forward/Backward THG power ratio generated at an interface as a function of excitation NA.

	Forward/Backward THG	
	XY interface	YZ interface
NA=0.5	3350	$> 10^{11}$
NA=0.9	749	
NA=1.4	134	

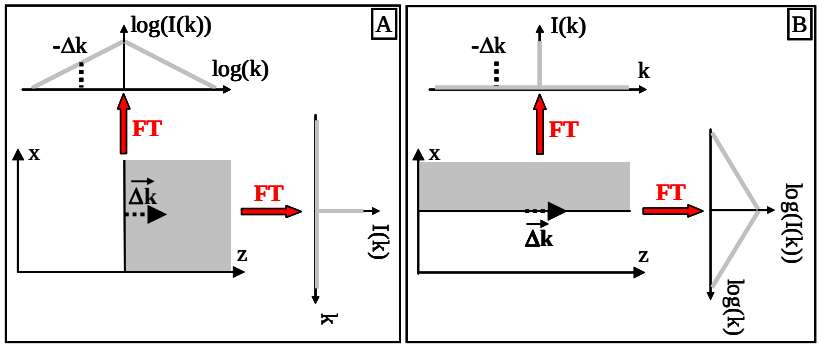

Fig. 2. Spatial frequency spectrum for an interface (A) perpendicular and (B) parallel to the excitation beam. In both cases, the large backward wave vector mismatch is not efficiently compensated by the sample structure.

3.2 Wave vector mismatch compensation in axially limited objects

This wave vector interpretation provides insight for determining which sample geometries can efficiently emit backwards: since $\|\Delta\mathbf{k}(\Theta=\pi)\|$ is typically 2 orders-of-magnitude larger than $\|\Delta\mathbf{k}(\Theta=0)\|$, a significant fraction of the signal will propagate backward only if the Fourier spectrum of the sample can efficiently compensate for large $\Delta\mathbf{k}$. This condition can be fulfilled either if the sample has a small size in the z direction (in which case the Fourier spectrum of the sample along that axis is relatively flat), or if the sample exhibits a periodic structure along z with the frequency required to compensate for $\Delta\mathbf{k}$.

Let us first consider the case of an object with a small z extension, e.g. (i) a slice with variable thickness e oriented perpendicular to $\mathbf{u}_z$, or (ii) a homogeneous sphere of variable diameter d centered on the focal point. The corresponding emission patterns, forward and backward TH signals are summarized on fig. 3. It is found that backward emission can represent a significant fraction of the total TH emission (at least 10% of the forward component) only for layer thicknesses e or bead diameters d smaller than 100 nm, corresponding to vanishingly small signals.

In the case of a thin slab (Figs. 1B and 3B1), the forward signal increases with thickness whereas oscillations are present in the backward emission as a function of e with a period $d_c = \pi/\Delta\mathbf{k}(\Theta=\pi)$. d_c corresponds here to the backward phase-matching length, i.e. the distance over which the fundamental and harmonic waves interact constructively, meaning that the number

#83793 - $15.00 USD Received 4 Jun 2007; revised 16 Jun 2007; accepted 22 Jun 2007; published 3 Jul 2007

of constructively interacting dipoles radiating in the backward direction is maximized when $e=d_c$. Such oscillations are not present in the forward direction in microscopy applications because (omitting the Gouy shift) $\pi/(3\mathbf{k}_\omega-\mathbf{k}_{3\omega})(\Theta=0) = l_c/2 \approx$ typ. 10 µm (where l_c is the coherence length of the medium) is larger than the axial extent of the excitation volume; here, excitation field distribution rather than dispersion limits signal creation. In the case of a sphere (Figs. 3C and 3B2), the lateral extent of the slice over which constructive interference occurs increases with the diameter of the object, resulting in increasing fringe amplitude in the backward direction. Finally we point out that in all cases, the backward- to forward- ratio is larger for high excitation numerical apertures as a result of increased $\|\mathbf{k}_g\|$ (Fig. 3C).

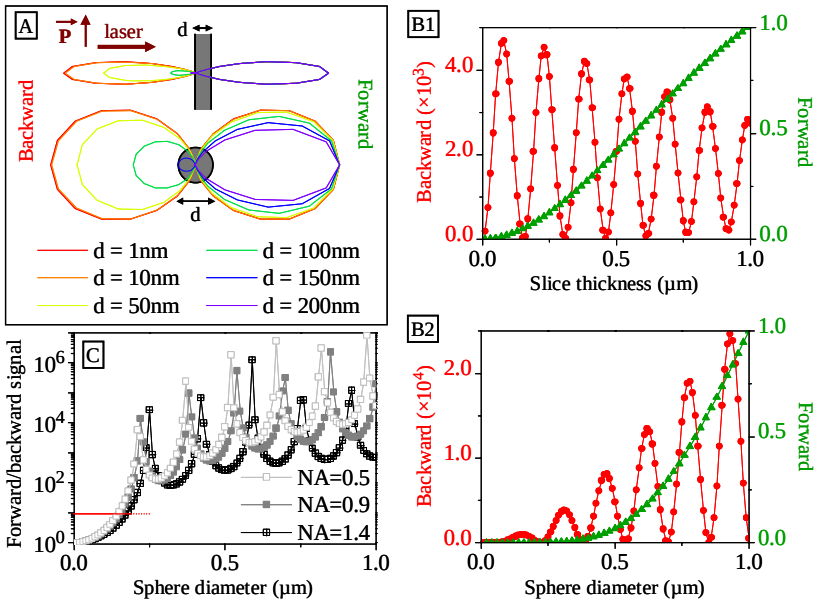

Fig. 3. TH emission patterns for a sphere and a thin slab at the focus of a Gaussian beam. (A) Normalized radiation patterns as a function of slab thickness (top) and sphere diameter (bottom). (B1) Slab: Forward (green triangles, right) and backward (red circles, left) emitted power as a function of thickness (NA=0.9). (B2) Sphere: forward (green triangles, right) and backward (red circles, left) emitted power as a function of diameter (NA=0.9). (C) Sphere: ratio of forward/backward emitted power as a function of diameter and excitation NA (semilog plot).

3.3 THG from a periodic pattern

These calculations indicate that homogeneous dielectric objects with reduced z-size will not emit significant amounts of backward TH power in practice. In the spirit of Mertz & Moreaux [23], we now consider the case of an inhomogeneous sample with nonlinear susceptibility exhibiting a sinusoidal variation along the z axis, i.e. exhibiting a unique non-zero spatial frequency $\pm 2\pi/\delta e$. The TH signal obtained when varying the period δe of this pattern is displayed in fig. 4. In order to compare the signal amplitude with the previous cases, the signal is here normalized to that obtained in the forward direction from a single interface perpendicular to the z axis (fig. 2A), a geometry that corresponds to the same number of emitters within the focal volume.

As previously, significant backward emission is obtained only when the sample wave vectors $\pm 2\pi/\delta e$ approach $\Delta\mathbf{k}(\Theta=\pi)$ (corresponding to $\delta e \approx 155$nm with our parameters) or $\Delta\mathbf{k}(\Theta=0)$. We note that the range of periodicities resulting in efficient backward emission is significantly broadened for a tightly focused beam as a consequence of excitation wave vector mismatch dispersion (due to the inclination of the wave vectors with respect of the optical axis), albeit with a smaller maximum signal amplitude. For the same reason, this maximum is

#83793 - $15.00 USD Received 4 Jun 2007; revised 16 Jun 2007; accepted 22 Jun 2007; published 3 Jul 2007

shifted towards greater δe values. The forward emitted component also exhibit interesting properties. First, the maximal amplitude is obtained for a value of δe smaller than the expected $l_c/2$ value prescribed by the coherence length of the medium, because the drop of excitation intensity far from the focal plane limits TH signal buildup. In line with this observation, a significant increase in the forward-propagating signal is obtained in the case of a weakly focused beam (corresponding to a larger focal volume). Contrasting with this situation, small values of δe (≤1μm) result in vanishing forward-emitted TH components and in efficient backward emission.

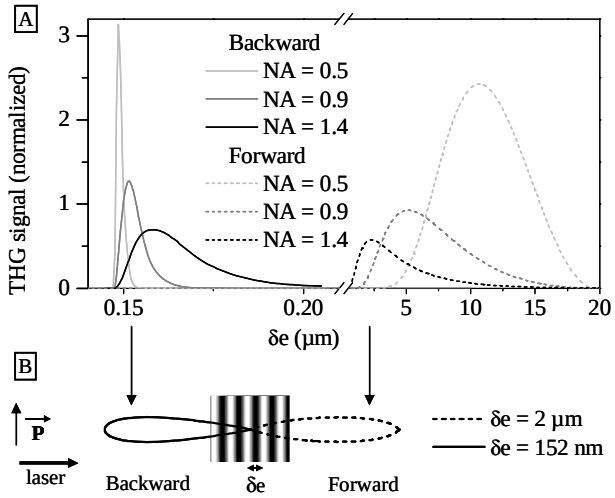

Fig. 4. Forward and backward emitted TH powers from an axially periodic (sine-like) object in a focused Gaussian beam, as a function of the spatial period δe. (A) Forward and backward emission for several NAs. (B) Radiation patterns for periodicities δe=2μm and δe=152nm (NA=0.9).

3.4 THG imaging of dielectric and metallic spheres

These predictions were confirmed experimentally by imaging individual polystyrene and metallic beads of various diameters embedded in agarose gels. Imaging was performed on a custom-built microscope [18, 30]. Excitation was performed with an optical parametric oscillator (APE, Berlin, Germany) delivering a 76 MHz, 200 fs pulse train at 1180 nm through a 0.9 NA water-immersion objective (Olympus, Tokyo, Japan). Forward-emitted TH light was collected through a ~1.2 NA condenser. Epi- and trans- signal were detected with photon-counting photomultiplier tubes (Electron Tubes, Ruislip, United Kingdom) and 100 Mhz counting electronics. Power incident on the sample was typically 50-80 mW, and pixel accumulation time was typically 5-50 μs. The bead concentration was chosen sufficiently low (typically 10^{-4} bead/μm^3) so as to avoid interference with surrounding objects.

First, we verified that for polystyrene beads, no signal could be detected in the backward direction (Fig. 5), as expected for a dielectric sample. Indeed, our calculations predict that a significant backward- to forward- ratio is obtainable only for beads smaller than 150 nm, and we could not detect significant TH emission from beads smaller than 300 nm within practical accumulation times. This arises from the highly nonlinear dependence of the THG signal on the bead diameter [30]: for beads smaller than the excitation volume and centered at the beam focus, the signal is expected to vary as the squared number of emitters, i.e. with the sixth power of the bead diameter (fig. 5A, dotted lines). This steep variation is corroborated by experiment (fig 5A, squares) and is responsible for the lack of visibility of small dielectric samples (and subsequent lack of epidetected signal).

#83793 - $15.00 USD Received 4 Jun 2007; revised 16 Jun 2007; accepted 22 Jun 2007; published 3 Jul 2007

The situation is markedly different in the case of metallic objects. Here, the previous analysis no longer holds since THG can arise from surface effects such as plasmon resonance [32], or a combination of surface and bulk effects [33]. A pure surface effect would be signed by a fourth-power dependence of the THG signal on the object size [32] and a backward-to-forward emission ratio approaching unity, and an interplay of surface and bulk effects is expected to produce an intermediate situation [33]. This is confirmed by our observations: we imaged 80 nm and 150 nm gold nanoparticles embedded in agarose gels and measured a power dependence on particle size of 5±0.5 (not shown), and a forward-to-backward ratio in the range 1-4 for 150 nm particles. This variability is likely related to heterogeneous particle shapes [34]. We note that transient heating of metal particles likely occurred upon illumination, as revealed by particle drifting within the gels during sustained imaging. We then imaged gels containing a mixture of 150 nm gold particles and 330 nm polystyrene particles (Fig. 5B). While all objects are visible in the trans-detected image, only some of them (metallic particles) are also detected in the epi channel. This observation indicates that metal nanoparticles could be used as convenient labels for epi-detected *in vivo* THG imaging.

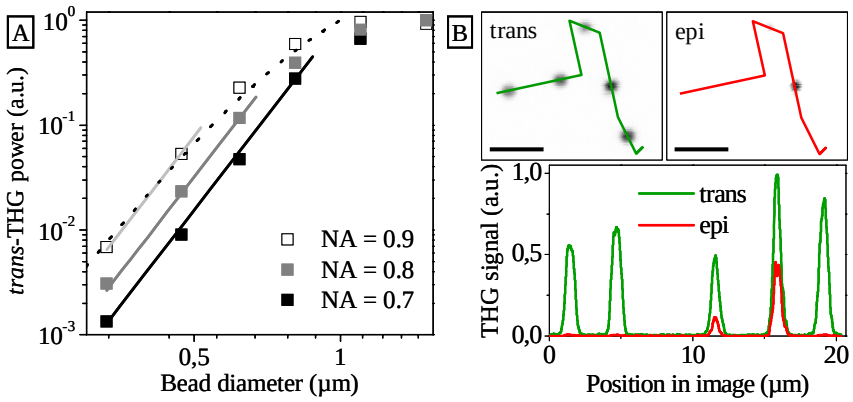

Fig. 5. Visibility of dielectric and metallic particles in THG microscopy. (A) Sixth-power dependence of the trans-THG signal on dielectric bead size. Squares: signal obtained from the center of individual polystyrene beads embedded in agarose and centered at the beam focus. Plain lines: sixth-power fits. Dotted line: numerical calculation for NA=0.9 and linear indexes of polystyrene (1.57 at 1180 nm and 1.61 at 393 nm). (B) Top: trans- and epi-detected THG images of a transparent gel containing 330-nm polystyrene beads and 150-nm gold particles. Gold particles are visible in the epi image, whereas polystyrene spheres are not. Bottom: profile through the broken lines indicated in the images. Scale bar is 3 µm. Excitation wavelength is 1180 nm.

4. Influence of elastic scattering in turbid samples

4.1 Epidetection from a scattering sample

The previous part of this study addressed the TH emission patterns of various isolated objects and showed that in most cases the absence of significant backward emission prevents TH epidetection from a transparent specimen. However the situation is different when imaging inside a thick tissue sample, because elastic scattering of the forward-emitted radiation by structures surrounding the imaged object may redirect a fraction of the harmonic light towards the tissue surface and the objective. Scattering of visible light in biological tissues is predominantly forward directed, with an anisotropy factor $g=\langle\cos\theta\rangle$ on the order of 0.9 to 0.95 [35], where θ is the scattering angle. Therefore the propagation direction of a photon after a single scattering event is strongly correlated to its initial direction, and randomization of propagation direction statistically occurs after a photon has travelled one reduced scattering mean free path $l_s' = l_s/(1-g) \approx 10\text{-}20\ l_s$ [35] where l_s is the scattering mean free path of TH light in the sample. As a result, photons must experience several tens of scattering events before

#83793 - $15.00 USD Received 4 Jun 2007; revised 16 Jun 2007; accepted 22 Jun 2007; published 3 Jul 2007

they can reach the tissue surface, even if the excitation beam is focused only a few microns under the surface (figure 6).

This situation is markedly different from the case of isotropic emission such as fluorescence, where a significant fraction of ballistic photons can escape the tissue at shallow imaging depths. Therefore experimental parameters affect epicollection efficiency differently in these two situations. First it should be noted that even at shallow imaging depths, epidetected TH light is exclusively diffusive rather than ballistic or "snake-like", so that the photons reaching the sample surface seem to originate from an extended light source in the focal plane. Therefore the detection efficiency should strongly depend on the field of view (e.g. the angular acceptance) of the collection optics: a low-magnification objective is expected to collect diffuse light more efficiently [10]. Secondly, even limited absorption of harmonic light by the tissue results in a dramatic drop of the collected fraction because TH photons must travel a distance at least on the order of $l_s' >> l_s$ before reaching the tissue surface. A significant epidetected signal can be obtained only if the absorption mean free path l_a is large compared to the distance travelled by photons in the tissue ($\sim l_s'$).

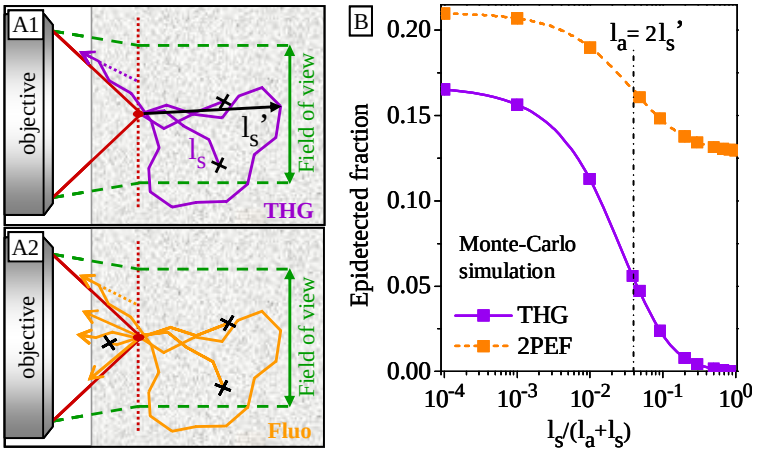

Fig. 6. Incidence of absorption and scattering on epidetection of backscattered harmonic light and multiphoton-excited fluorescence from a turbid medium. (A1) Detection of backscattered forward-emitted light (THG). (A2) Detection of light from an isotropic source (2PEF). (B) Epidetected fraction of THG and 2PEF as a function of tissue albedo (g=0.92, l_s=25µm, NA=0.95, field of view=1000µm, working distance=2mm, sample thickness=2500µm).

We corroborated this analysis by Monte Carlo simulations of THG and 2PEF light propagation inside a homogenous thick scattering slab, following [36], and by experiments on model and tissue samples. The simulation algorithm consisted in the following: photons were generated from a point source located near the surface of a semi-infinite scattering slab. Initial directions were chosen isotropic (2PEF) or forward-directed (THG). Photons then underwent a random walk, with scattering events every l_s and scattering angles taken from a Henyey-Greenstein distribution with anisotropy factor g. 5×10^6 random walks were simulated for each situation. Trajectories were weighted according to their length and to the absorption mean free path of the medium. Photons were then ray-traced through the backward or forward collection optics, described by their respective numerical aperture and acceptance angle (or field of view).

4.2 Incidence of absorption and scattering on epidetection

We estimated the epidetected fraction of emitted power as a function of the scattering and absorption mean free path of light in the tissue. Figure 6B displays collected fractions as a function of the absorption mean free path in the tissue. As expected, the epidetected TH signal drops rapidly when l_a becomes comparable with l_s'. Setting $l_a = 2\ l_s'$ results in a drop of ≈66%

#83793 - $15.00 USD Received 4 Jun 2007; revised 16 Jun 2007; accepted 22 Jun 2007; published 3 Jul 2007

of the detected TH power, very close to the expected value of 1-1/e≈63%. On the contrary, absorption has less impact on 2PEF epidetection: even in a strongly absorbing tissue ($l_a \approx l_s$) epidetected power is only reduced by about one third, because surface photons initially directed toward the focusing objective are not affected by absorption.

4.3 Incidence of the collection optics on epidetection

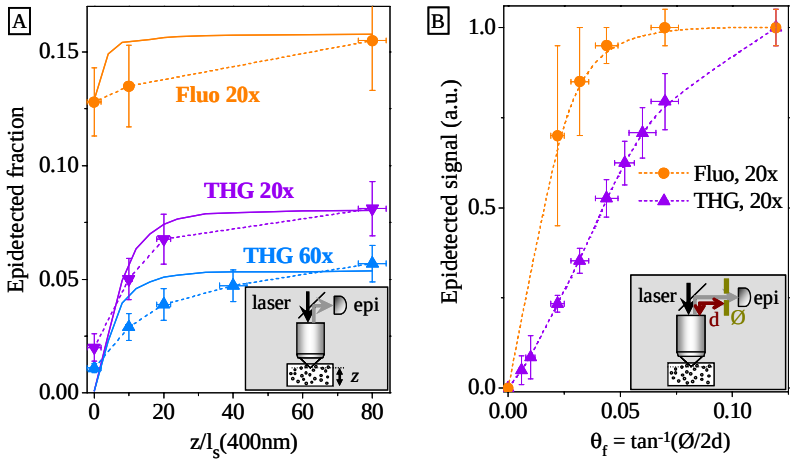

Fig. 7. Incidence of the microscope angular acceptance (field of view) on epidetection of THG and 2PEF from a turbid medium. (A) Measured epidetected fraction as a function of slab thickness (symbols and dotted lines), and corresponding Monte Carlo simulations (plain lines) for two different objectives (60×, 0.9NA and 20×, 0.95NA). Simulations assume that $l_s^{(400)}$=25µm and that the angular field of view is clipped to 0.13 rad (half-angle) by the collection optics. (B) Measured epidetected THG and 2PEF signal at the center of the field, as a function of the angular acceptance of the collection optics.

Simulations also confirm a strong dependence of the collected THG power on the field of view (i.e. angular acceptance) of the collection optics. Figure 7A presents estimates of the epidetected fractions of THG and 2PEF for a source located near the surface of a slab, as a function of slab thickness (expressed in scattering mean free paths). Simulations were run for several sets of collection optics with similar NAs (0.9) but different field-of-view radii r_f, assuming that the effective angular acceptance θ_f^{eff} of the collection optics[10] was ultimately limited to ~0.13 rad by the collection lens (which mimicked the situation in our microscope). We remind that in the absence of collecting lens, θ_f is related to the field of view radius r_f and objective focal length f by $\theta_f \approx \tan^{-1}(r_f/f)$ [10, 11]. Epi-THG relies exclusively on the detection of multiply-scattered light, which reaches the tissue surface far from the optical axis, hence the strong impact of the field of view even at shallow imaging depths. We confirmed this analysis experimentally by recording epidetected 2PEF and THG images of (blue-fluorescent) 520 nm polystyrene microspheres deposited on top of a scattering gel consisting of nonfluorescent 800 nm beads embedded in agarose. We used scattering slabs of thicknesses ranging from 0.2 to 2 mm obtained using a vibrating microtome. Gel scattering mean free path $l_s^{(400)}$ for 400-nm light was estimated by two independent means. First, Mie theory was used to predict $l_s^{(400)}$ from the beads size and concentration [37]. Second, $l_s^{(1200)}$ was estimated from the measurement of ballistic laser beam attenuation by a thin slice of gel, and $l_s^{(400)}$ was deduced from Mie theory. Scattering anisotropy was also calculated from Mie theory, which yields g=0.92 at 400 nm. Those measurements led to an estimate of $l_s^{(400)}$ = 25±10 µm for the gel used. The epidetected TH fraction was then estimated by normalizing the epidected signal by the trans-signal level measured in the same geometry for beads deposited on top of a non-scattering slab.

Figure 7A shows the epidetected THG signal as a function of slab thickness for two objectives of comparable numerical apertures (0.95 vs 0.9) but different magnifications (20× and 60×). For comparison, we also plotted the fluorescence signal epidetected through the 20×

#83793 - $15.00 USD Received 4 Jun 2007; revised 16 Jun 2007; accepted 22 Jun 2007; published 3 Jul 2007

objective. Experimental data and simulations exhibit both qualitative and quantitative agreement. In particular: (i) no epi-THG is obtained from a thin sample, as opposed to the case of fluorescence where the epicollected fraction is ½(1-cos θ_{NA}); (ii) increasing the field of view (i.e. decreasing the magnification) while keeping a constant NA enhances the backscattered light collection efficiency.

Finally, we explored the effect of aperture clipping in the collection path resulting in a reduced angular acceptance. Figure 7B shows the relation between the effective angular acceptance and the epidetected signal level. For this experiment, we recorded epidetected 2PEF and THG generated at the center of the field of view as a function of effective θ_f, by placing an aperture of variable diameter Ø in front of the collection lens (see inset in Fig. 7B). These data again confirm that epidetected 2PEF at the surface of a scattering slab is largely ballistic, whereas epidetected THG is essentially diffusive (i.e. consists of multiply scattered forward-emitted light). The non-saturating THG detection curve also indicates that the angular acceptance is limited by the collection lens in our system, resulting in sub-optimal detection of backscattered diffuse light. Additional simulations predict that >20% epidetection efficiency is expected from a nonabsorbing medium with a 20×, 0.95 NA, unclipped collection path (not shown).

4.4 Epidetection in biological samples

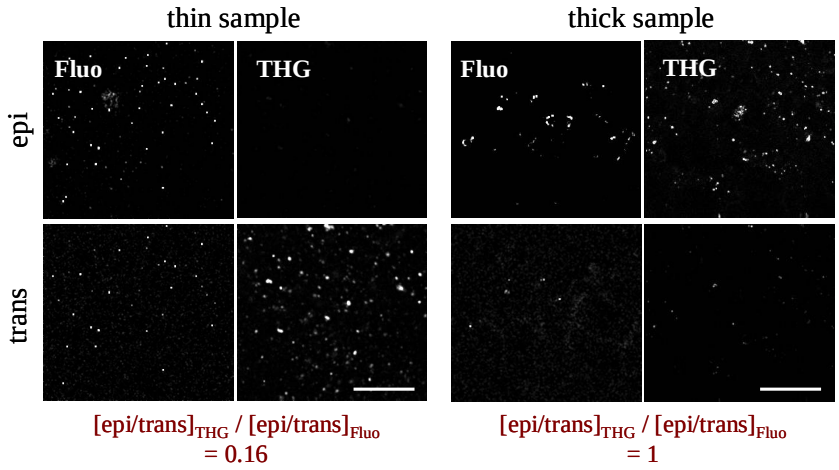

Fig. 8. Trans- and epi-detection of endogenous THG and multiphoton-excited fluorescence from a washed fresh lung tissue sample. Epi-THG imaging is possible only in thick areas, as opposed to epi-fluorescence. Epi/Trans image pairs were acquired simultaneously. THG and fluorescence images were recorded at different locations. Acquisition time, 10 µs/pixel. Scale bar, 50 µm.

Finally, we illustrate the consequence of these observations for biological tissue imaging. We recorded epi- and trans- THG/Fluorescence images of fresh washed rat lung tissue samples upon 1200 nm excitation. Images were recorded near the surface of thin areas (close to the tissue border) and of 1-mm thick areas. As discussed in a previous study, THG contrast in this type of sample originates principally from lipid structures [18]. Many of these objects are also fluorescent, although they exhibit rapid bleaching.

We consistently made the following observations, illustrated by typical images in Fig. 8: (i) THG was detected only in the trans channel in thin samples, and mostly in the epi-channel in thick samples; (ii) multiphoton-excited fluorescence was readily detected in the epi-channels from both thin and thick samples. We introduce the parameter $\beta = [epi/trans]_{THG} / [epi/trans]_{Fluo}$ as a normalized measure of the epi/trans ratio. We measured a six-fold increase in β between thin and thick samples, which again illustrates the role of scattering in THG epidetection.

#83793 - $15.00 USD Received 4 Jun 2007; revised 16 Jun 2007; accepted 22 Jun 2007; published 3 Jul 2007

5. Discussion

This study provides a basis for determining experimental situations where TH signals can be epidetected from biological samples. Typical dielectric objects fail to provide a significant backward directed TH radiation because of phase mismatch. The weakness of third-order susceptibilities of biological samples can only be overcome by the coherent excitation of a large number of scatterers - or possibly by resonance effects. This is in contrast with the case of e.g. second-harmonic generation from collagen fibrils, where direct backward emission (presumably from the fibril surface) is observed owing to the higher efficiency of harmonic generation in these structures.

Backward TH emission is however observed in the case of metallic structures such as gold or silver nanoparticles, where harmonic generation is at least partially a surface effect. We note that such particles could easily be functionalized and used as exogenous probes in thick tissue, thus allowing background-free specific imaging with convenient epidetection. Efficient backward emission should also be possible from structures exhibiting a periodic pattern with spatial frequencies enabling quasi-phase matching in the backward direction. However this situation is unlikely to occur in biological samples since it requires not only a regular spatial organization with a given period, but also large nonlinear susceptibility variations. We also note that such a sub-micrometric structure cannot enhance forward-emitted harmonic radiation and does not explain reports of THG by mitochondria [38]. Instead, we propose that mitochondria signals stem from the contrast with the surrounding cytoplasm and from the presence of concentrated hemoproteins, possibly exhibiting resonantly-enhanced nonlinear susceptibilities for near-infrared excitation [39]. Another mechanism that could result in (limited) coherent backward emission is internal reflection due to refractive index mismatch within a sizeable structure. This effect was pointed out for CARS microscopy [40] and may also lead to a few percent of THG back-reflection in specific geometries.

Our study also shows that THG epidetection is generally possible when the imaged structure is embedded in a scattering, non-absorbing tissue with thickness greater than the reduced scattering mean free path. The data presented here indicate that this effect likely accounts for the epidetected endogenous signals reported in previous articles [18, 20, 29]. Experiments and simulations show that >20% of the total created TH signal may be detected from weakly absorbing thick tissues, provided that signal collection is optimized by using a low-magnification, high NA objective and by making sure that the microscope collection pathway does not clip scattered photons before they reach the detector. These optimization criteria also apply to CARS and SHG microscopies. We stress that THG epidetection requires that photons travel a distance inside the tissue significantly larger than their scattering mean free path without being reabsorbed. THG microscopy is usually performed with excitation light in the 1100-1500 nm range corresponding to a harmonic wavelength of 370-500 nm, a range where linear absorption in tissues is usually strongest due to hemoglobin and other absorbers. Further increasing the excitation wavelength would likely result in sample heating by water absorption, whereas decreasing the excitation wavelength yields increased two- and three- photon absorption and associated phototoxicity. Therefore, epidetected THG microscopy based on endogenous contrast is feasible mostly in weakly vascularized tissues such as skin, or alternatively on washed or perfused tissues.

In conclusion, this study provides guidelines for understanding TH signal creation in biological samples and for practical implementation of epidetected THG microscopy.

Acknowledgments

We thank L. Combettes for providing us with the lung tissue samples, and J.-M. Sintes and X. Solinas for assistance in microscope design. This work was supported by the Délégation Générale pour l'Armement.

#83793 - $15.00 USD Received 4 Jun 2007; revised 16 Jun 2007; accepted 22 Jun 2007; published 3 Jul 2007